Self-organized gold nanoparticles on SiO₂ surface nanopatterns induced by MeV ion implantation

C.F. Cruz-Garcia, M.A. Garcia, E. Flores-Romero, J. Rickards, L.R. de la Vega, J. Cañetas-Ortega,
J.G. Morales-Morales, L. Rodríguez-Fernández

Ion implantation at MeV energies leads to the formation of surface nano-patterns on diverse kinds of materials, such as metals, dielectrics, and semiconductors. Furthermore, under oblique irradiation, the implanted ions are preferentially deposited on the crests of such patterns. Based on previous experimental results, in this work the formation of gold nanoparticles is produced and found to be organized onto prepatterned surfaces as produced by 1.8 MeV Au ion implantation on SiO2 substrates at an impinging angle of 45°. The ion implantation was performed with an ion beam current of 400 nA for a total ion fluence between 0.2×10^{17} cm^{-2} and 2.0×10^{17} cm^{-2}. After implantation, to assist gold nanoparticle nucleation, substrates were annealed at 1000 °C. The surface morphology and topography of the implanted substrates were analyzed by atomic force microscopy (AFM) and scanning electron microscopy (SEM), respectively. For the lowest fluences ($0.4 - 0.8 \times 10^{17}$ cm^{-2}), the formation of isolated surface structures on a flat background was observed whose morphology mimics the exoskeleton of a bug. According to SEM-EDS analysis, the formation of gold nanoparticles on the exoskeleton of the bugs was observed. For intermediate fluences ($0.8 - 1.4 \times 10^{17}$ cm^{-2}), a ripple background now appears and begins to surround the bugs. At the highest fluences ($1.4 - 2.0 \times 10^{17}$ cm^{-2}), the surface shows only a ripple pattern. In this last case, the gold nanoparticles are formed along the crests of the surface ripples. Finally, the optical absorption of the samples (except the one corresponding to the lowest fluence) shows the presence of a localized surface plasmon resonance (LSPR) in the wavelength region of 520 - 540 nm, suggesting the presence of gold nanoparticles.

Introduction

It has been reported that ion implantation can induce the formation of surface nanopatterns (dots, ripples, wrinkles, etc.) on a wide variety of materials, such as glasses (insulators) [1,2], metals [3] and semiconductors [4]. Since the first reported case until now, surface pattern formation by ion implantation has attracted attention within the scientific community due to its potential application as a technique to fabricate functionalized surfaces in several emerging nanotechnology industries [5]. For example, it has been reported that surface nanopatterns induced in glass by ion implantation can improve the efficiency of solar cells [6] and in nanophotonics [7]. It is currently known that, given a material, the physical characteristics of surface patterns (such as their amplitude and wavelength) depend on the experimental parameters of ion implantation (type and energy of ion, ion flow and substrate temperature) [5,8]. In this sense, surface patterns with desired characteristics may be fabricated. However, in the case of implantation with MeV ions, the dependence between the characteristics of the surface patterns and the implantation parameters is not yet fully understood [1,9,10].

From a physical point of view, such patterns are produced by morphological instabilities caused by the competition between surface roughness and surface smoothing mechanisms [5,11]. The first successful model proposed by Bradley and Harper (BH) [11], the ion erosion acts as a surface roughness mechanism, while thermally activated surface diffusion as a smoothing mechanism. Currently, the BH model has been modified to include near-surface mechanisms incorporating ion implantation and surface mass redistribution [12-14], whose effects are known to be relevant for the case of ion implantation at keV to a few MeV of energies [2]. The effect of ion implantation near the surface consists mainly in a surface swelling which ultimately influences the pattern formation [15]. Regarding the mass redistribution mechanism, this can be described as a viscous flow confined at the surface (on a mesoscopic scale) driven by a residual stress induced by the ion beam [16,17]. The BH model and its modifications were formulated for the case of amorphous surfaces (or those that become amorphous under ionic irradiation, such as semiconductors [18] or crystalline SiO₂ [19]), therefore, they are not applicable to surfaces that under ionic irradiation keep a crystalline structure, such as metals [5].

On the other hand, metallic nanostructures (nanoparticles, nanorods, nanoparticle arrays, etc.) with plasmonic properties have aroused given their unique optical responses, such as strong light absorption [20], Rayleigh scattering [21] and surface-enhanced Raman scattering (SERS) [22,23]. These unique optical properties are due to the strong interaction between plasmonic nanostructures and an incident light through localized surface plasmons (LSP), which are the collective oscillation of light-excited free

C. F. Cruz-Garcia ✉ [ORCID], E. Flores-Romero, J. Rickards, J. Cañetas-Ortega, J. G. Morales-Morales, L. Rodríguez-Fernández [ORCID]
Instituto de Física, Universidad Nacional Autónoma de México, Mexico City, 04510, Mexico.

M. A. Garcia [ORCID]
Fac. de Ciencias, Universidad Nacional Autónoma de México, Mexico City, 04510, Mexico

L. R. de la Vega
Acad. de Matemáticas, Univ. Autónoma de la Ciudad de México, Mexico City, 07160, Mexico.

electrons. When the oscillation frequency of free electrons matches that of incident light, localized surface plasmon resonance (LSPR) is established. The properties of LSPR depend, in general, on the size, shape, and composition of plasmonic nanostructures, as well as the environment where these nanostructures are embedded [24,25]. Regarding the composition, most research in this field has focused on gold plasmonic nanostructures, especially due to their good biocompatibility, satisfactory stability, and multiplex functionality [26]. Due to current technological demands, the search for more efficient and low-cost methods to fabricate plasmonic nanostructures remains an open problem [27,28].

This work studies the formation of plasmonic gold nanoparticles as a product of a two-stage process. Ion implantation followed by a thermal annealing to synthetize nanoparticles. Au ion implantation is performed on SiO_2 substrates at an oblique angle of incidence with the formation of surface exoskeleton akin to bugs, surface ripples and their subsequent evolution to wrinkles. The formation of plasmonic gold nanoparticles is found to be arranged on surface nanopatterns induced on SiO_2 by 1.8 MeV Au ion implantation, following a thermal annealing at 1000 °C. The formation of the nanopatterns is explained through the mechanisms of ionic erosion, mass redistribution and ion implantation, while the formation of the gold nanoparticles is explained by a geometric shadowing mechanism together with the effects of thermal annealing. Due to the high degree of control of the experimental parameters during ion implantation (resulting in surface nanopatterns with desirable properties), the work presented here shows an efficient method for the formation of plasmonic metal nanoparticle arrays with possible applications in SERS-sensor [29].

Experimental details

High-quality commercial fused silica glass (amorphous SiO_2, Nippon Silica Glass – NSG-OZ SiO_2) substrates were implanted with 1.8 MeV Au^{+2} ions using the 3 MV Pelletron accelerator (NEC 9SDH-2) at the Instituto de Física of the Universidad Nacional Autónoma de México. The ion current was kept at 400 nA corresponding to an ion flux of 1.0×10^{13} ions cm^{-2} s^{-1} within a vacuum of 10^{-7} torr at room temperature. The ion beam impinged at a 45° angle with respect to the surface normal over a square area of 0.25 cm^2 centered on the silica glass substrates. The total ion implantation fluences Φ ranged from 0.2×10^{17} ions cm^{-2} to 2.0×10^{17} ions cm^{-2}. After implantation, all samples were thermally annealed at 1000 °C in air for 1 hour. In previous annealing tests, it was found that 1000 °C was the threshold thermal annealing temperature for the synthesis of distinguishable nanoparticles. On the other hand, the choice of this annealing temperature does not compromise the thermal stability of the samples, since their annealing point| is 1180 °C.

The surface morphology and topography of the implanted substrates was characterized by optical microscopy (OLYMPUS BH2-UMA), scanning electron microscopy (SEM, JEOL JSM-7800F) and atomic force microscopy

(AFM, JEOL SPM-4210) before and after thermal annealing. AFM data analysis was carried out with the help of the open-source software Gwyddion [30]. To determine variations in the elemental composition of the surface, energy dispersive X-ray spectroscopy (EDX) was performed using an Oxford XMaxN50 detector coupled to the JEOL JSM-7800F electron microscope. Finally, an Ocean Optics SD2000 dual-channel UV-visible spectrophotometer was used to collect optical absorption spectra in the 300 to 800 nm wavelength range, using unpolarized light.

Results and discussion

Before thermal annealing, AFM-SEM characterization showed a flat surface without any distinguishable feature for the lowest fluence ($\Phi = 0.2 \times 10^{17}$ ions cm^{-2}). Figure 1 shows SEM and AFM micrographs (figure insets) of the implanted surface of SiO_2 substrates before thermal annealing for the fluences $\Phi = 0.4 \times 10^{17}$ ions cm^{-2} to 2.0×10^{17} ions cm^{-2}. The ion beam direction is from left to right, on the surfaces shown in the micrographs. Both surface probing techniques (SEM and AFM) show a similar surface structurization as a function of ion fluence. For $\Phi = 0.4 \times 10^{17}$ ions cm^{-2}, the formation of craters on a flat background, whose rims are elongated in the direction of the ion beam, can be observed in Figure 1a. Therefore, $\Phi = 0.4 \times 10^{17}$ ions cm^{-2} is the threshold ion fluence for the formation of ion implantation-induced surface features. For the next two fluences
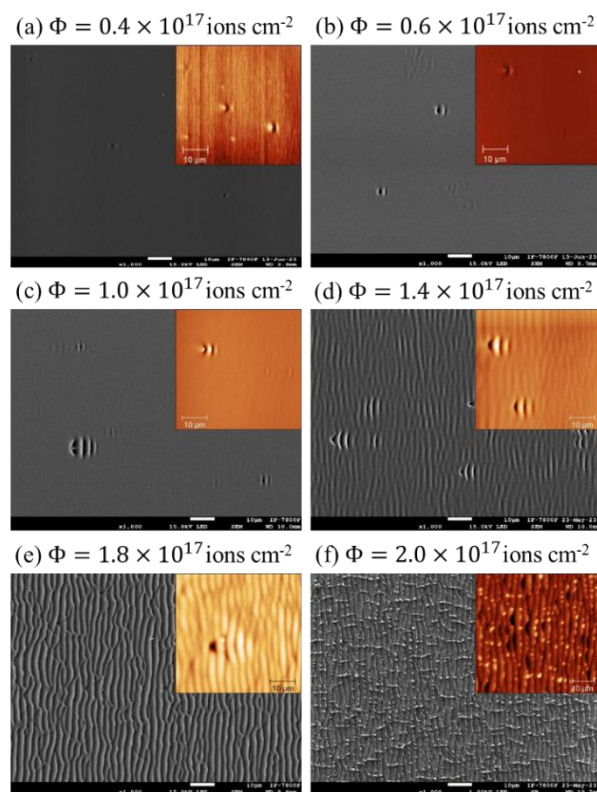

Figure 1. SEM and AFM (figures insets) micrographs of Au ion implantation of SiO_2 substrates for increasing ion fluence. The beam direction is from left to right on all micrographs. SEM micrographs were taken at 1000X magnification while AFM micrographs at 25 μm × 25 μm scanning areas.

Φ = 0.4 and 0.6 $\times 10^{17}$ ions cm^{-2}, these craters evolve into structures that imitate the segmented exoskeleton of a bug (Figures 1b and 1c). The largest diameter of bugs is between 6 - 8 μm and is aligned with the direction of the ion beam. Thus, a notable surface morphological change occurs at the fluence Φ = 1.4 $\times 10^{17}$ ions cm^{-2}. Indeed, as seen in Figure 1d, for this fluence the bugs increase in size (∼10 μm), which shows a wavy exoskeleton and the formation of ripples perpendicular to the ion beam and can be observed in the superficial background. Subsequently, in the next fluence (Φ = 1.8 $\times 10^{17}$ ions cm^{-2}), the ripples grow in amplitude until the bugs disappear (Figure 1e) and finally evolve into a wrinkle-like pattern (Figure 1f) at the highest fluence (Φ = 2.0 $\times 10^{17}$ ions cm^{-2}). From AFM micrographs, the amplitude of the bugs and ripples was estimated to be on the order of a couple hundred of nanometers (Figures 1b-1e), while the amplitude of the wrinkles was estimated to be on the order of 1 μm (Figure 1f). The wavelength (spatial periodicity) of both ripples and wrinkles is about 3 μm.

Crater formation at the lowest ion fluence is the initial process for surface pattern formation and is due to the ion implantation process, see Figure 1a. This is believed to be a consequence of surface erosion and described by the slowing down of ions in the target material. Regarding the crater rim, an EDS-SEM analysis found that it was composed mainly of gold atoms. Therefore, the shape of the craters observed in Figure 1a results from the local deposition of gold by the ion beam along this direction. Craters on the flat surface act as an exceptionally large height fluctuation that gives rise to bug-like structures with the increase of ion fluence (proportional to the ion implantation time). In an optical analysis (not shown here), it is observed that craters/bug-like grow preferentially on surface irregularities. This explains how craters and bug-like structures form in locally and isolated confined positions on the surface.

Considering the Bradley-Harper model, along with the current extensions, the weight of the mechanisms of ionic erosion, mass redistribution and ion implantation within the framework of ripple pattern formation was determined. According to this model, the temporal evolution of the height field $h(x,y,t)$ on the substrate surface due to ion irradiation is given by the following linear partial differential equation:

$$\frac{1}{J}\frac{\partial h}{\partial t} = C_{11}\frac{\partial^2 h}{\partial x^2} + C_{22}\frac{\partial^2 h}{\partial y^2} - K\nabla^4 h \qquad (1)$$

where J is the ion flux (1/cm^{2}s), and K represents the thermally activated surface diffusion coefficient (nm^4/s) representing a relaxation mechanism at the surface. The surface physical processes contribute to the height equation of motion (1) through the weight coefficients C_{ii} (i =1, 2) in the following way:

$$C_{ii} = C_{ii}^{ero} + C_{ii}^{mred.} + C_{ii}^{imp} \qquad (2)$$

where terms on the right side of equation (2) correspond to surface erosion, mass redistribution and ion implantation processes. To obtain a quantitative estimate, the above coefficients can be estimated as $C_{ii}^{ero} \approx Y_0\Omega\,a_{ero}$ [31], $C_{ii}^{mred} \approx \Omega\delta$, and $C_{ii}^{imp} \approx \Omega\,\alpha_{imp}\,\beta_{imp}/a_{imp}$. Here, Y_0 is the average sputtering yield of a flat surface at normal incidence,

Table 1. TRIM estimated parameters for the computation of coefficients C_{ii}^{ero}, $C_{ii}^{mred.}$ and C_{ii}^{imp} (i = 1, 2) in equation (2). These values correspond to the case of amorphous SiO$_2$ implanted with 1.8 MeV Au ions at normal incidence. All quantities are average values.

Erosion			Implantation		
Penetr. depth	Longi. straggling	Lateral straggling	Penetr. depth	Longi. straggling	Lateral straggling
a_{ero} (nm)	α_{ero} (nm)	β_{ero} (nm)	a_{imp} (nm)	α_{imp} (nm)	β_{imp} (nm)
355.8	180.1	79.6	451.1	80.8	55.1

CV (mass redistribution/transport)			
Recoil depth	Vacancy depth	Knockon events	Recoil distance
d_R (nm)	d_V (nm)	N (ion^{-1})	δ (nm ion^{-1})
340.3	340.1	17052	3410.4

Ω is the substrate atomic volume, a_{ero} (a_{imp}) is the average depth for energy deposition (implantation), α (β) is the corresponding longitudinal (lateral) straggling length for surface erosion (ero) or implantation (imp), and δ is the average travel distance of the recoil atoms. These parameters were estimated by TRIM [32] for the ion implantation conditions of this work at normal incidence and are shown in Table 1. Using the estimated values of Table 1, it is found
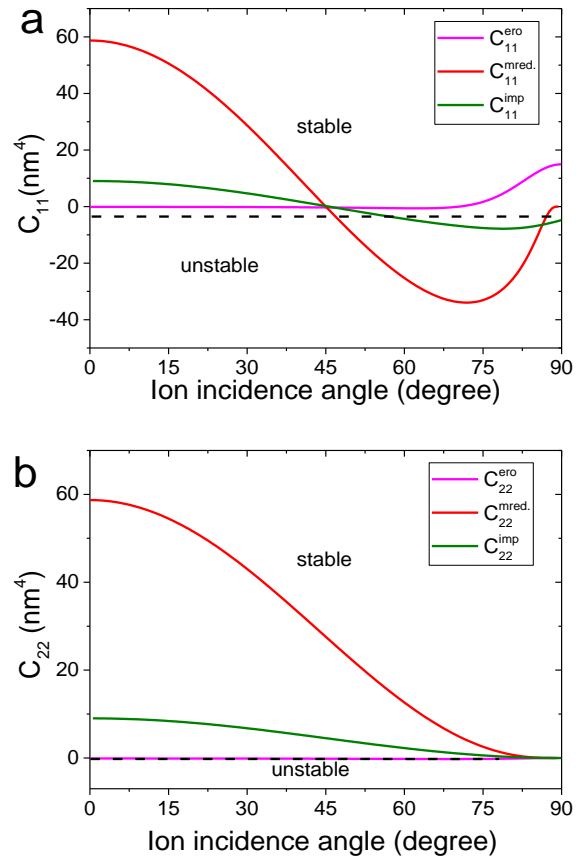
Figure 2. Weight coefficients C_{ii}^{ero}, $C_{ii}^{mred.}$ and C_{ii}^{imp} dependence on the angle of incidence θ for (a) the x direction (along the ion beam) and for (b) the y direction (perpendicular to the ion beam) from equation (2).

that $C_{ii}^{ero} \approx 55.5$ nm^4, $C_{ii}^{mred.} \approx 68.2$ nm^4, and $C_{ii}^{imp} \approx 0.20$ nm^4 for the ion implantation conditions of the current work. Therefore, compared to ion erosion and redistribution, the contribution of implantation is negligible.

The dependence of the coefficients C_{ii}^{ero}, C_{ii}^{mred}, and C_{ii}^{imp} on the angle of incidence θ of the ion beam is shown in Figure 2a for the $x = 1$ direction (along the ion beam) and in Figure 2b for the $y = 2$ direction (perpendicular to the ion beam). While Figure 2a predicts a critical angle of incidence at 45º and higher angles for ripple pattern formation, Figure 2b predicts stability on the *y*-direction at all angles of incidence. Moreover, the transition from the ripple pattern to the wrinkle pattern observed in the final ion fluence (see Figure 1f) can be explained as the result of surface swelling due to ion implantation [7]. Based on other studies, where a wrinkle-like pattern was observed on SiO$_2$ surfaces implanted with low-energy ions (0.5-1.2 keV) [33-34], the amplitude of the wrinkles is expected to stabilize while their wavelength shows an increasing behavior starting from the ionic fluence $\Phi = 2.0 \times 10^{17}$ ions cm^{-2}. That is, the evolution of the patterns is expected to enter a non-linear temporal regime for fluences higher than $\Phi = 2.0 \times 10^{17}$ ions cm^{-2} (compared to a linear regime, where the amplitude of the patterns grows with the ionic fluence, but their wavelength is constant [11]).

Thermal annealing of implanted substrates does not modify surface nanostructures, however gold nanoparticles are synthesized along the crest of bug-type structures as observed in Figure 3a, for a fluence of 1.4×10^{17} ions cm^{-2}. As the ion fluence is increased, Au nanoparticles align along the crest of ripples at the ion fluence of 1.8×10^{17} ions cm^{-2} (Figure 3b). Lastly, at the fluence of 2.0×10^{17} ions cm^{-2}, a higher homogeneity and density of Au nanoparticles occurs

Figure 4. a) An initial SiO$_2$ flat surface is implanted with an Au ion beam at an incidence angle of 45°. b) After certain fluence, a ripple pattern emerges and is able to shadow the ion beam, c) resulting in the preferential implantation of Au ions on ripple crests. d) As a consequence of this shadowing effect, after thermal annealing the synthesis of Au nanoparticles on the ripple crests occurs.

along the crest of surface wrinkles (Figure 3c). Nanoparticles initial size begin at around 10-15 nm and increases to 150 nm for higher fluence implantation.

The alignment of Au nanoparticles can be explained by the graphical representation given in Figure 4. An initial flat SiO$_2$ surface is implanted with an Au ion beam at an incidence angle of 45° (see Figure 4a). At an incubation ion fluence of 1.4×10^{17} ions cm^{-2} a ripple surface pattern emerges whose amplitude can overshadow the ion beam, as shown in Figure 4b. In Figure 4c the shadowing effect occurs at high fluence where ions are preferentially implanted on the crests of the ripple pattern. Subsequently, Figure 4d shows that after thermal annealing of implanted substrates, synthesis of Au nanoparticles at ripple crests occurs. SEM-EDX analysis was used to verify that atomic Au was accumulated at the crests for bug-like, ripple, and on wrinkle-like surface structures (see Figure 3d). The synthesized nanoparticles occur along the crests of the ripples, therefore, small nanoparticles on a crest are expected to grow under Ostwald ripening [35]. The formation of nanoparticles with a size of around 120 nm closely surrounded by smaller nanoparticles (size ~ 10 - 15 nm), as observed in Figures 3b and 3c, supporting Ostwald ripening.

The functionalization of surface nanostructures for optical applications can be elucidated by probing the response of surface plasmons. Figure 5 shows the optical absorption spectrum of thermal annealed substrates as a function of the ion fluence. Except for the lowest fluence, in all cases the localized surface plasmon resonance (LSPR) can be observed around 520 - 540 nm. The presence of the LSPR band around 520 nm [36] indicates the presence of Au synthesized nanoparticles.

Figure 5 shows that, for the intermediate fluences, where surface bug-like and bug-like + ripple structures appear, the LSPR is well defined and its intensity is lower than in comparison with the LSPR corresponding to the last two fluences, where only surface ripples and wrinkles appear. It is also observed that the LSPR of the last two fluences is slightly red shifted, compared to the LSPR of the intermediate fluences. This LSPR behavior can be attributed to the formation of nanoparticles larger than 100 nm at the
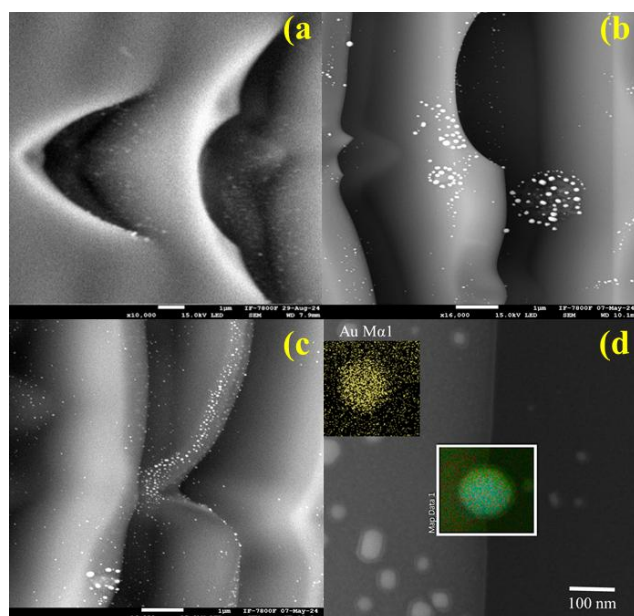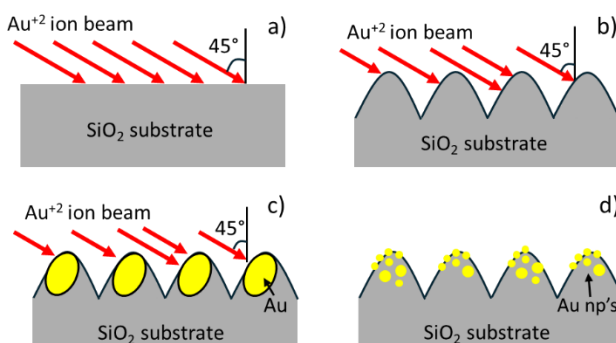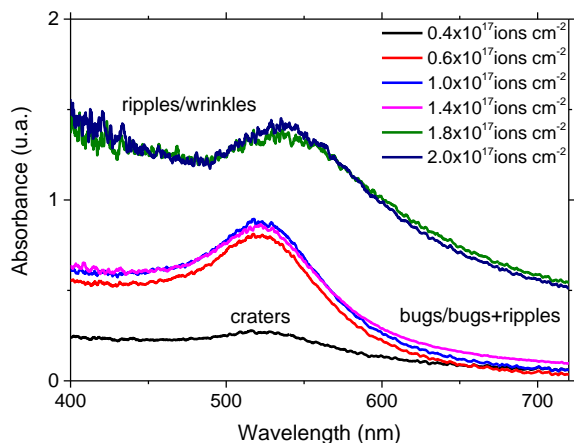

Figure 3. Subsequent thermal-annealing formation of Au nanoparticles on the crests of (a) bug-like structures (for ion fluence $\Phi = 1.4 \times 10^{17}$ ions cm^{-2}), (b) align along the crests of the ripples (ion fluence $\Phi = 1.8 \times 10^{17}$ ions cm^{-2}) and (c) surface wrinkles (ion fluence $\Phi = 2.0 \times 10^{17}$ ions cm^{-2}). (d) Synthesized Au nanoparticles are verified by SEM-EDX analysis.

Figure 5. Optical absorption spectrum for implanted and thermal annealed substrates in relation to the ion fluence.

two highest fluences (see Figures 3b-3d). In this case, contributions from higher-order electronic oscillations would be predominant [36], resulting in a less sharp peak, higher intensity, and the red shift of the LSPR observed for the last two fluences.

Conclusions

Surface morphology of SiO_2 substrates implanted with a 1.8 MeV Au ion beam, at an incidence angle of 45°, shows to be dependent on the ion fluence, ranging from $\Phi = 0.2$ - 2.0×10^{17} ions cm^{-2}. At the lowest fluence, the formation of surface craters on a flat background was observed, which evolved over ion fluence into bug-like surface structures. Then, at intermediate fluences ($\Phi = 1.0$ - 1.4×10^{17} ions cm^{-2}, a ripple pattern was formed on background that grew in amplitude over an increased ion fluence until it surrounds and outshines bug-like structures. While, at higher ion implantation fluences this ripple pattern evolved into a wrinkle-like pattern at fluence $\Phi = 2.0 \times 10^{17}$ ions cm^{-2}. Thermal annealing at 1000 °C, after implantation, lead to the formation of Au nanoparticles on the crests of the bug-like, ripple, and wrinkle-like structures, as observed by SEM-EDX. The size of the nanoparticles was between 10 and 120 nm, and their synthesis was explained by a geometrical shadowing effect and Ostwald ripening. The growth of ripples and wrinkles is a result of surface erosion, mass redistribution and ion implantation processes. The mass redistribution process was found to be the major contributing factor, followed by surface erosion, and lastly, the implantation process was negligible. Finally, the absorption spectrum of the samples showed localized surface plasmon resonance (LSPR) at 520 - 540 nm, except for the sample corresponding to the lowest fluence.

Acknowledgements

References

[1]. C.F. Cruz-Garcia, J Rickards, M.A. Garcia, L.R. de la Vega, J Cañetas-Ortega, J.G. Morales-Morales, L. Rodríguez-Fernández, *Phys. Scr.* **98**, 105956 (2023).

[2]. M.A. Garcia, R. Martínez-Cervantes, J. Rickards, J. Cañetas-Ortega, J.G. Morales-Morales, L.R. de la Vega, L. Rodríguez-Fernández, *Nucl. Instrum. Methods Phys. Res. B* **550**, 165304 (2024).

[3]. U. Valbusa, C. Boragno, F. Buatier de Mongeot, *J. Phys. Condens. Matter* **14**, 8153 (2002).

[4]. J. Muñoz-García, L. Vázquez, M. Castro, R. Gago, A. Redondo-Cubero, A. Moreno-Barrado, R. Cuerno, *Mater. Sci. Eng. R* **86**, 1 (2014).

[5]. R. Cuerno, J.S. Kim, *J. Appl. Phys.* **128**, 180902 (2020).

[6]. C. Mennucci, S. Del Sorbo, S. Pirotta, M. Galli, L.C. Andreani, C. Martella, M.C. Giordano, F. Buatier de Mongeot, *Nanotechnology* **29**, 355301 (2018).

[7]. M.C. Giordano, F. Buatier de Mongeot, *Adv. Mater.* **30**, 1801840 (2018).

[8]. W.L. Chan, E. Chason, *J. Appl. Phys.* **101**, 121301 (2007).

[9]. M.A. Garcia, R. Gago, J. Rickards, R. Trejo-Luna, J. Cañetas Ortega, L.R. de la Vega, L. Rodríguez-Fernández, *J. Phys. Condens. Matter* **30**, 274005 (2018).

[10]. S.K. Srivastava, K.G.M. Nair, R. Kamalakannan, M. Kamruddin, B.K. Panigrahi, A.K. Tyagi, *AIP Conf. Proc.* **1447**, 741 (2012).

[11]. R.M. Bradley, J.M.E. Harper, *J. Vac. Sci. Technol. A* **6**, 2390 (1988).

[12]. B. Davidovitch, J. Aziz, P. Brenner, *Phys. Rev. B* **76**, 205420 (2007).

[13]. B. Davidovitch, J.M. Aziz, M.P. Brenner, *J. Phys. Condens. Matter* **21**, 224019 (2009).

[14]. R.M. Bradley, H. Hofsäss, *J. Appl. Phys.* **120**, 074302 (2016).

[15]. B. Rauschenbach, *Low-Energy Ion Irradiation of Materials: Fundamentals and Application*, 1st ed. (Springer Cham, 2022) p. 250-251.

[16]. C.C. Umbach, R.L. Headrick, K.C. Chang, *Phys. Rev. Lett.* **87**, 246104 (2001).

[17]. M. Castro, R. Cuerno, *Appl. Surf. Sci.* **258**, 4171 (2012).

[18]. H. Gnaser, *Low Energy Ion Irradiation of Solid Surfaces*, 1 st ed. (Springer-Verlag, 1999) p. 153-204.

[19]. L. Douillard, J.P. Duraud, *Nucl. Instrum. Methods Phys. Res. B* **107**, 212-217 (1996).

[20]. W. Ou, B. Zhou, J. Shen, C. Zhao, Y.Y. Li, J. Lu, *iScience* **24**, 101982 (2021).

[21]. P. Long Truong, X. Ma, S.J. Sim, *Nanoscale* **6**, 2307 (2014).

[22]. J. Liu, H. He, D. Xiao, S. Yin, W. Ji, S. Jiang, D. Luo, B. Wang, Y. Liu, *Materials (Basel)* **11**, 1833 (2018).

[23]. T.Y. Jeon, D.J. Kim, S.G. Park, S.H. Kim, D.H. Kim, *Nano Convergence* **3**, 18 (2016).

[24]. J.P. Cordero-Santiago, A. Crespo-Sosa, *Photonics Nanostructures: Fundam. Appl.* **51**, 101051 (2022).

[25]. A. Chhatre, P. Solasa, S. Sakle, R. Thaokar, A. Mehra, *Colloids Surf. A Physicochem. Eng. Asp.* **404**, 83 (2012).

[26]. X. Ou, Y. Liu, M. Zhang, L. Hua, S. Zhan, *Mikrochim. Acta* **188**, 304 (2021).

[27]. H. Duan, T.Wang, Z. Su, H. Pang, C. Chen, *Nanotechnol. Rev.*

11, 1 (2022).

[28]. P. Mandal, S. Sharma, *Renew. Sustain. Energy Rev.* **65**, 537 (2016).

[29]. M. Saini, S. Augustine, M. Ranjan, T. Som, *Appl. Surf. Sci.* **512**, 145703 (2020).

[30]. D. Nečas, P. Klapetek, *Central Eur. J. Phys.* **10**, 181 (2012).

[31]. M.A. Garcia, J. Rickards, R. Cuerno, R. Trejo-Luna, J. Cañetas-Ortega, L.R. de la Vega, L. Rodríguez-Fernández, *Phys. Rev. Applied* **8**, 064027 (2017).

[32]. J.F. Ziegler, M.D. Ziegler, J.P. Biersack, *Nucl. Instrum. Methods Phys. Res. B* **268**, 1818 (2010).

[33]. A. Keller, S. Facsko, W. Möller, *Nucl. Instrum. Methods Phys. Res. B* **267**, 656 (2009).

[34]. M. Teichmann, J. Lorbeer, F. Frost, B. Rauschenbach, *Nanoscale Res. Lett.* **9**, 439 (2014).

[35]. H. Amekura, N. Kishimoto, Fabrication of Oxide Nanoparticles by Ion Implantation and Thermal Oxidation. In: *Toward Functional Nanomaterials*, Ed. Z. Wang (Springer, 2009) p. 1-75.

[36]. X. Huang, M.A. El-Sayed, *J. Adv. Res.* **1**, 13 (2010).